A Novel Localised Coherence Rule Delay-And-Multiply Algorithm Towards Long-Range Ultrasound Imaging with Narrow Field-of-View pMUTs

Gaia Giubilei, Mantalena Sarafianou *Member, IEEE*, David Sze Wai Choong *Member, IEEE*, Duan Jian Goh *Member, IEEE*, and Yul Koh, *Member, IEEE*

***Abstract*— This work proposes an innovative signal post-processing algorithm for long-range ultrasound imaging by using a narrow Field-of-View (narrow-FoV) Lead Zirconate Titanate (PZT) piezoelectric Micromachined Utrasonic Transducer (pMUT) array. Two 3×3 mm^2 dies of a 1D-array pMUT, whose resonant frequency is 6.5 MHz, consisting of 18-channels, were employed for this demonstration. The entire system has 18-channels by electrically combining two columns of pMUT membranes as one to increase the transmission power with the cost of narrowing FoV. In this work, experimental testing using single and multiple 5 mm diameter spherical reflectors at various arrangements was performed to validate the 2D imaging capabilities of the developed pMUT array with the proposed image reconstruction algorithm achieving a 1.5 mm lateral resolution.**

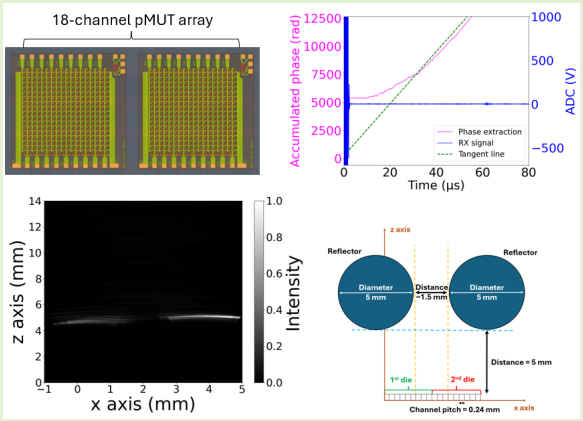

***Index Terms*— piezoelectric Micromachined Ultrasonic Transducer (pMUT), receive beamforming, ultrasonic imaging**

I. Introduction

To-date, ultrasonic transducers have been used in a wide range of applications including ranging [1], [2], diagnostic imaging [3], non-destructive testing (NDT) [4], [5], and mid-air haptics [6] among others. Although traditional ultrasonic transducer arrays, which are based predominately on bulk piezoelectric ceramics, have been broadly used for imaging, they have several limitations. First, high-resolution imaging is typically associated with actuation at high frequencies. However, this is difficult to achieve with standard piezoceramics, due to the difficulty in scaling down their physical dimensions [7]. Second, for specific imaging applications such as NDT and endoscopy, the need for an array with compact size that is able to fit in small enclosures makes bulk piezo materials unsuitable [8]. Such design constraint could be addressed with Micro-Electromechanical System (MEMS) technology, and specifically with piezoelectric Micromachined Ultrasonic Transducer (pMUT) arrays given their small form factor, low-cost, and matured fabrication processes [9].

The development and application of pMUTs over the past decade have revolutionized ultrasound imaging, offering advantages such as compactness, seamless integration with electronic systems, superior impedance matching and high-resolution capabilities at lower driving voltages [10]. The fabrication technology for Lead Zirconate Titanate (PZT) pMUTs is to-date well-established and it offers a high piezoelectric coupling coefficient, which makes it desirable for imaging applications [2], [11]. In addition, physical vapor deposition process for PZT is recently being matured further, which accelerates the commercialization of PZT pMUT by lowering the process cost.

Along with the development of the MEMS transducer technologies, there is demand for innovative solutions for algorithmic image reconstruction to fully exploit the potential of

This paper manuscript was submitted for review on XX November 2024. This research was supported by Agency for Science, Technology and Research (A*STAR) under the “Piezo Specialty Lab-in-Fab 2.0” programme (Grant No. I2301E0027).

Ms. Gaia Giubilei is with the Institute of Microelectronics (IME), Agency for Science, Technology and Research (A*STAR), Singapore and the Politechnico di Torino, Torino, Italy.

Dr. Mantalena Sarafianou (email: Mantalena_Sarafianou@ime.a-star.edu.sg), David Sze Wai Choong, Duan Jian Goh, and Dr. Yul Koh (email: Yul_Koh@ime.a-star.edu.sg) are with the Institute of Microelectronics (IME), Agency for Science, Technology and Research (A*STAR), Singapore. For any additional information pertaining to this paper please contact us at: Mantalena_Sarafianou@ime.a-star.edu.sg or Yul_Koh@ime.a-star.edu.sg.

pMUTs in medical as well as industrial applications. To-date, the study of the impact of different image reconstruction algorithms in conjuction with pMUTs is limited. In [12], the 2D imaging capability of Silicon-On-Nothing (SON) Scandium-doped Aluminium Nitride (ScAlN) pMUT linear arrays was experimentally validated considering Common Source Method (CSM) for the actuation and Delay-and-Sum (DAS) processing for image reconstruction. In [13], the authors extended their previous work reported in [12] demonstrating a 5mm lateral resolution at 2.5cm range in immersion with a 2D SON ScAlN pMUT array actuated with transmit (TX) focusing at long-range. In [14], the authors reported a novel Double-Stage Delay-Multiply-and-Sum (DS-DMAS) beamforming algorithm specifically targeting non-destructive testing (NDT), which yields Signal-to-Noise ratio (SNR) and resolution enhancements. [15] and [16] reported high-resolution imaging (100-200μm), which was limited to short ranges of a few millimeters. Although the results are impressive with acoustic pressure preserved for a couple of millimeters axially, this is at the cost of burdensome mechanical scanning in [15] and the usage of a waveguide in [16]. In [17], the authors conducted a comprehensive benchmarking exercise of existing image reconstruction algorithms including DAS, DMAS and several known variations for these post-processing methods considering again TX focusing as the actuation mechanism.

Although pMUTs are promising devices towards medical ultrasound imaging, they demonstrate a low transmit (TX) pressure [18]. To address this issue TX beamforming (i.e., TX focusing), which is an actuation mechanism that can attain improved lateral resolution by narrowing the TX beam width at a specific focal point, could be used. However, multiple scannings are potentially required to obtain acceptable imaging results, when the location of the object-of-interest is unknown, which would take a toll on the data rate attained by the hardware control (i.e, FPGA, MIC, etc). An alternative approach to overcome the low TX pressure issue would be to combine multiple pMUT membranes to boost the output pressure. In such a solution, the transducer aperture size would increase resulting in a narrow Field-of-View (FoV).

Specifically for narrow-FoV pMUT arrays (with a sharp natural focus) for short- and mid-range imaging applications, the combination of TX focusing and DMAS image reconstruction algorithms would result in reconstructed images with high SNR, which may not reflect the actual contour of the reflector. This is due to the fact that DMAS processing, which aims at improving signal coherence through receive (RX) signal multiplication, would only be valid for neighbouring array channels with intersecting coverage. If the coverage areas of the channels do not overlap, the signals will not be coherent and multiplying them would not improve the overall image quality. Hence, it is anticipated that classical DMAS processing (along with existing variants) would result in image resonstructions with poor lateral resolution. To fully exploit the potential of narrow-FoV pMUTs in ultrasound imaging, new signal processing algorithms must be developed that account for their limited FoV. These algorithms should enhance the quality of reconstructed images, while minimizing computational time and enabling real-time medical imaging.

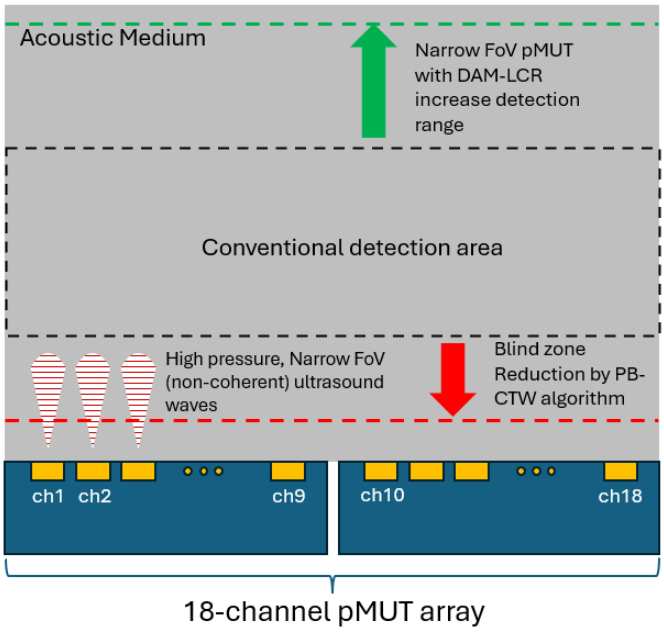

Fig. 1. Illustration of the proposed work: Extending the detectable range by combining narrow-FoV pMUTs with an innovative image reconstruction algorithm (DAM-LCR), while reducing the blind zone through a novel algorithm for crosstalk suppression (PB-CWT).

On this token, the work presented here aims to address the existing gap in immersion imaging using narrow FoV pMUT arrays for short- and mid-range imaging applications as illustrated in Figure 1. This work introduces a novel signal processing methodology for image reconstruction, which is based on increasing RX signal coherence through receive signal multiplication (and will be referred to Delay-and-Multiply (DAM) processing) based on the proposed Localised Coherence Rule (LCR) using PZT pMUT arrays with a narrow (30^o) FoV. Furthermore, this work investigates the performance of the well-known DMAS multiplier-2-signals (denoted as DMAS2) processing and DMAS multiplier-3-signals (denoted as DMAS3) processing when modified with the proposed LCR condition. Moreover, a novel calibration technique is proposed in this work based on the Continuous Wavelet Transform (CWT) to suppress the blind zone by eliminating the undesired signal contribution of crosstalk. In this way, the imaging ability of the array extends closer to it (as seen in Fig. 1).

This work will conduct an assessment of the proposed algorithms' computational efficiency and their enhancements in imaging performance (in terms of lateral resolution and image SNR metrics). This work will provide a comparative analysis of the proposed signal post-processing algorithms against established image reconstruction algorithms, such as conventional DAS and classical DMAS processing, by correlating fully-simulated datasets with experimental data from in-immersion testing. This benchmarking exercise is designed to systematically bridge the theoretical predictions with the empirical observations, thus, providing a robust framework for evaluating the efficacy and reliability of the proposed novel imaging algorithms within the domain of narrow-FoV pMUT-

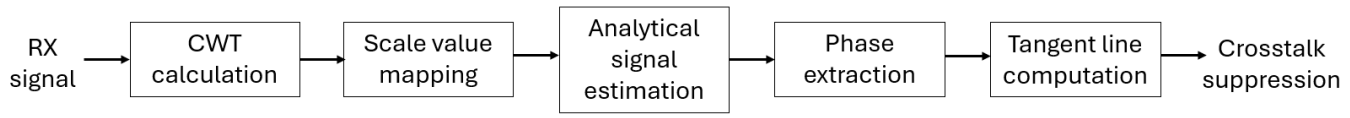

Fig. 2. Block diagram of the proposed signal pre-processing methodology, PB-CWT, for crosstalk suppression

based short- and mid-range ultrasound imaging. Through simulated and measured data an impressive lateral resolution of 1.5mm is demonstrated employing a 18-channel pMUT array consisting of two dies and an aperture as small as 10mm×10mm.

The paper is organized as follows: Section II describes the actuation mechanism and the two proposed novel algorithms for: (i) crosstalk suppression (PB-CWT), and (ii) image reconstruction (DAM-LCR). In addition, two algorithmic variants are introduced in this work considering the Localised Coherence Rule (LCR) for the classical DMAS2 and DMAS3 procesing, namely DMAS2-LCR and DMAS3-LCR respectively. Section III presents the pMUT design and its key characteristics quantified through hydrophone measurements. In Section IV, the experimental settings are described in detail, and Section V discusses the experimental evaluation of the proposed method for crosstalk suppression. Section VI presents the analysis of results from the experimental data post-processed using the proposed DAM-LCR and the variants DMAS2-LCR and DMAS3-LCR against the classical DAS, DMAS2 and DMAS3 processing algorithms in order to benchmark performance in terms of lateral resolution, SNR and computational cost. Lastly, conclusions are drawn in Section VII.

II. Imaging Scheme Description

A. Data Acquisition Method

In order to actuate the N elements (i.e., channels) of the pMUT array, the CSM is used, originally reported in [19]. In CSM, all the array elements are excited simultaneously, which results in the creation of a plane wave that propagates into the imaging domain. All the channels of the pMUT array are at once actuated and then the array switches from Tx mode into RX mode (without any waiting period) for the recording of the RX signals. The collected RX data would contain undesired early-time contributions (crosstalk, electrical coupling, ringing, etc.) along with echoes from the scattering of waves on the reflector surface.

B. Phase-based Continuous Wavelet Transform Method for Crosstalk Suppression

Initially, the RX data need to be pre-processed to suppress crosstalk, which involves the unintentional transfer of acoustic or electrical signals between adjacent pMUT channels. Traditionally, crosstalk is mitigated through calibration. First, a measurement of the domain is captured without the reflector present (reference measurement) [14]. The RX data from the reference measurement are then substracted from the measured data with the reflector present [12], [13]. This method often is not completely effective since it results in residual crosstalk, leading to image distortion.

The authors recently proposed a Sliding Window Autocorrelation (SWA) method for crosstalk suppression [20], which calculates the similarity correlation $G(\tau)$ between a template signal (i.e., a measurement of the domain taken without the reflector present) and the signal of interest (i.e., a measurement taken with the reflector's position being unknown). This method was experimentally evaluated using a PZT pMUT array in pulse-echo configuration in immersion reducing the blind zone within the first 10 mm [20]. Since approximately 1 cm of detectable short-range is not usable for imaging purposes, a more effective pre-processing method is needed to reduce the blind zone to less than 1 cm. Furthermore, the method proposed in [20] is strongly dependant on the signal variability (both in terms of amplitude and phase), deeming it as susceptible to a large variation in the resulting (suppressed) blind zone from 1 cm to 2-3 cm.

The Wavelet Transform is a powerful mathematical operation, which to-date has been extensively explored for image processing [21], audio classification [22] and pMUT-based ultrasonic ranging [23]. This work introduces a novel signal processing approach for crosstalk suppression: Phase-Based Continuous Wavelet Transform (denoted as PB-CWT in the remaining of this document). The proposed pre-processing methodology relies on the application of the Continuous Wavelet Transform (CWT) to a received signal, resulting in the definition of the CWT coefficients. Given their complex mathematical nature, these coefficients are characterised by the magnitude and phase. The proposed methodology uses this phase information to determine the cut-off point in order to set the early-portion of the received signals to zero, eliminating any undesired signal contributions. Preconditioning of signals using CWT has been applied in biosensing towards the monitoring of optical signal changes through phase shift detection in the optical signals [24]. However, to the best of the authors' knowledge, CWT has not yet been applied to suppress crosstalk in ultrasound signals using pMUTs. Figure 2 outlines the processing steps of the proposed PB-CWT method.

Initially, the CWT is computed for every raw RX signal, and the corresponding complex wavelet coefficients are calculated using the following equation:

$$T_w(\alpha,\tau) = \frac{1}{\sqrt{\alpha}} \int_{-\infty}^{+\infty} x(t)\psi^*(\frac{t-\tau}{\alpha})dt \qquad (1)$$

where parameter $T_w(\alpha,\tau)$ provides a measure of the match between the RX signal, $x(t)$, and a scaled and delayed version of the (mother) wavelet, $\psi^*(t)$, where parameters α and τ are the scale and time delay respectively and * refers to the complex conjugate operator. There is a wide variety of mother wavelets available in the literature; however, in this

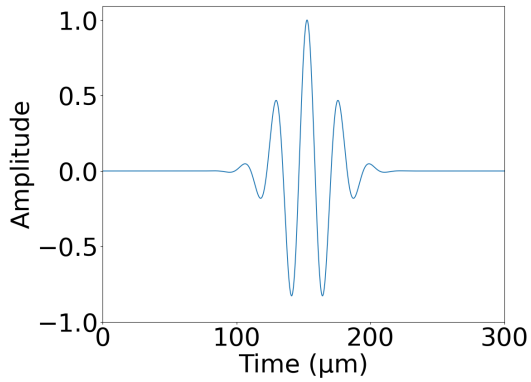

Fig. 3. Mother wavelet illustration: Real part of the complex Morlet wavelet

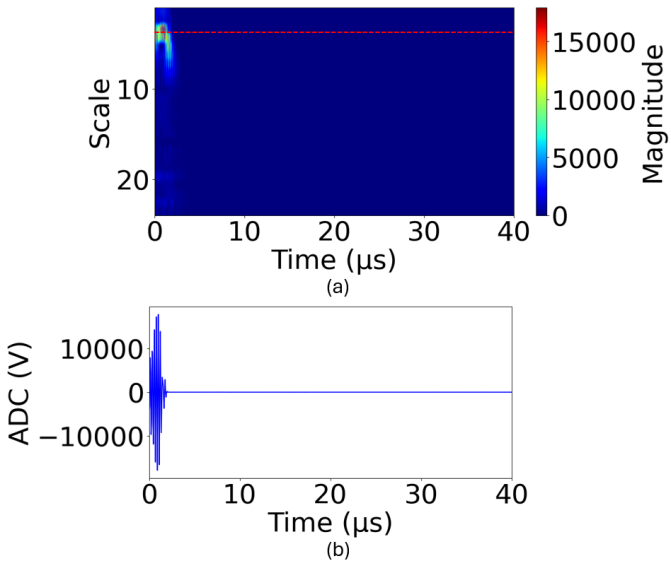

Fig. 4. (a) 2D scalogram of the absolute value of the wavelet coefficients across scale and time values for an example RX signal considering a scale range from 0 to 40, (b) 1D scalogram of the selected CWT coefficients, $T_w(\alpha = \alpha_{max}, \tau)$, expressed by eq. 2

work, the Morlet mother wavelet was selected empirically based on the method's performance and repeatability. As a rule of thumb, a mother wavelet would be selected based on its similarity to the waveform of the generated RX signal accounting for its discrepancy from the generated actuation signal (i.e., microwave sensing systems generate Gaussian-like excitation waveforms and, thus, a complex Gaussian wavelet would be suitable [25]). The Continuous Wavelet Transform coefficients represent the degree of similarity between the wavelet and the received signal. From an empirical point of view, among all wavelets, the Morlet Wavelet is the one that most closely match the RX signal (e.g., the shape of the echo signal considering ringing, attenuation profile, signal distortion, etc.). Thus, by choosing this wavelet as the mother wavelet, the accuracy of CWT pre-conditioning would be maximised. Figure 3 illustrates the Morlet mother wavelet, while Figure 4(a) presents a 2D scalogram, which displays the absolute values of the CWT coefficients across scales α and time delays τ.

According to the developed method, the maximum value of the scalogram (as defined from eq. 1) is identified and the value of the scale, α_{max}, corresponding to this maximum value is determined. Using this scale value the CWT coefficient $x(t)$ associated is selected. Observing Fig. 4(a), the above operation would result in the selection of the horizontal line indicated in red in Figure 4(a) (i.e. across a specific value for the scale, α_{max}, considering all the time values) as expressed below:

$$T_w(t) = T_w(\alpha = \alpha_{max}, \tau) \tag{2}$$

Figure 4(b) demonstrated the output of eq. 2.

The analytical form of $T_w(t)$, denoted as $z(t)$, is then computed using the following equation:

$$z(t) = \Re T_w(t) + j\mathcal{H}(\Re T_w(t)) \tag{3}$$

where $\Re T_w(t)$ refers to the real part of the complex function $T_w(t)$, the $\mathcal{H}$ operation denotes the Hilbert Transform applied to the real part of the complex function $T_w(t)$. From the analytical signal $z(t)$, which is a complex sequence with a magnitude and a phase component, the phase at every time instant, t, is extracted as follows:

$$\phi(t) = \arctan^{-1}\left(\frac{\mathcal{H}(\Re T_w(t))}{\Re T_w(t)}\right) \tag{4}$$

The phase values are unwrapped into a continuous representation using their period-complementary values (i.e., if the absolute difference between two consecutive phase angles is greater than π, 2π is added or subtracted from the phase value, choosing the adjustment that brings it closer to the preceding value). With the knowledge of the accumulated phase trend, a linear model is fitted to the phase data to extract the tangent line to the accumulated phase curve. The intersection of the tangent line with the x-axis is used as the cutoff point to set to zero the early-portion of the RX signal to suppress the crosstalk. Figure 5 illustrates an example of the proposed PB-CWT method implementation for crosstalk removal to assist towards the reader's understanding: for an example RX signal plotted in blue, the accumulated phase curve is plotted in magenta, with the tangent line plotted in green (dashed line). The crosstalk suppression is achieved by setting the input RX signal to zero from the beginning ($t = 0$) up to the previously defined intersection point (denotes as crosstalk zeroing in Fig. 5).

C. Proposed DAM-LCR Methodology for Image Reconstruction

For every pre-conditioned RX signal $x_i(t)$, the envelope, $\bar{x}_i(t)$, is initially computed using the Hilbert Transform and then passed to the proposed RX beamforming algorithm to reconstruct a two-dimensional (2D) image. Figure 6 illustrates a schematic of the implementation of the proposed DAM-LCR methodology for image reconstruction. For every i-th pMUT array channel, an updated dataset $y_{DAM-LCR_i}$, is defined as per the following equation:

$$y_i(t) = \bar{x}_{i-1}(t) * \bar{x}_i(t) * \bar{x}_{i+1}(t) \tag{5}$$

where for the first (and last, i.e., N-th) channel the updated signal, $y_1(t)$ (and $y_N(t)$, respectively) is set to zero. The

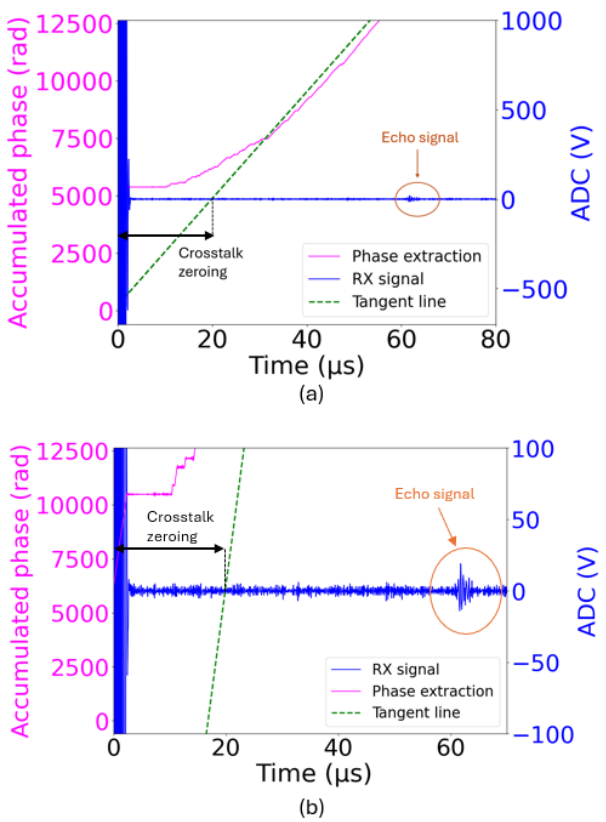

Fig. 5. (a) Example of the proposed PB-CWT method implementation for crosstalk removal, (b) zoom-in view of the example depicted in (a)

reason is that there is only a pair multiplication for the first and last channels, rather than a triplet multiplication. For the 2-nd to $N-1$-th channels of the pMUT array, each updated signal is obtained by multiplying a triplet of RX signals considering three consecutive channels, all at one-pitch distance apart, e.g., for the second channel the updated signal would be obtained by multiplying the RX signals from the first, second and third channels.

This operation, referred to as the Localised Coherence Rule (LCR), is expected to enhance signal coherence specifically for pMUT arrays with restricted FoV, thus significantly improving the ultrasound imaging quality. More specifically, multiplying signals from only first neighbors (i.e. one-pitch-distance apart) exploits the higher correlation of closely positioned RX channels, assuming that RX signals from adjacent channels are more likely to be relevant to each other due to similar directivity patterns, footprint of restricted FoV.

Once crosstalk is removed from the RX datasets, the signal envelopes are calculated by applying the Hilbert Tranform to the RX signals and computing the absolute value prior to signal multiplication by the DAM-LCR beamforming algorithm (eq. 5). The reconstructed image corresponds to energy intensity values distributed over a 2D Cartesian grid of finite-spaced points (denoted as pixels p), which could map all the possible reflector locations in the imaging domain [21]. In the case of classical DAS processing, for every pixel, all the RX updated signal envelopes, y_i, would be evaluated in the time-delay $2d_{pixel(rx)}/c$ and then summed with the operation

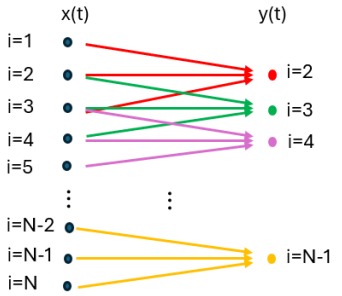

Fig. 6. Implementation of the proposed DAM-LCR image reconstruction algorithm

expressed by the following formula:

$$I(p(x_{pixel}, z_{pixel})) = |\sum_{i=1}^{N} y_i(\frac{2d_{pixel(rx)}}{c})| \quad (6)$$

where $d_{pixel(rx)}$ maps the Euclidean distance from the pixel to the RX channel - with multiplication by 2 indicating the round-trip distance and c is the speed of sound in the propagation medium (i.e., for FC-70, c=687m/sec).

D. LCR Implementation on DMAS2 Processing Algorithm

In the classical DMAS beamforming considering multiplications between pairs of RX signals (denoted as DMAS2 for the remaining of this document), the signal envelopes are multiplied together considering all RX pairs combinations prior to the summation [26]. This can be expressed as follows:

$$y_i^{DMAS2}(t) = \sum_{i=1}^{N-1} \sum_{j=i+1}^{N} x_i(t)x_j(t) \quad (7)$$

where $x_i(t)$, and $x_j(t)$ represent the envelopes of the RX signals by the i-th, and j-th array channel, respectively. In the case of array channels with a wide Field-of-View (FoV), the DMAS2 algorithm improves the image quality with respect to the classical Delay-and-Sum by taking into account the spatial coherence of the received signals. However, from the point of view of pMUTs with a narrow FoV, restriction of the RX envelope pair combinations is needed to ensure that signal coherence is not inadvertently cancelling out features-of-interest due to the lack of coverage across all the array channels. By introducing the Localised Coherence Rule (LCR), this method is modified as per the equation below:

$$y_i^{DMAS2-LCR}(t) = \sum_{i=1}^{N}(x_i(t)x_{i-1}(t) + x_i(t)x_{i+1}(t)) \quad (8)$$

where $x_{i-1}(t)$, $x_i(t)$, and $x_{i+1}(t)$ represent the envelopes of the RX signals by the $i-1$-th, i-th, and $i+1$-th array channel, respectively. In the expression of equation 8, the terms within the summation are defined as per the respective pMUT array arrangement. Specifically, the first channel (i = 1) does not have a preceding channel, and thus, the updated signal for the first channel would consider only the multiplication with signal from the next (i+1) channel, converging to $x_i(t)x_{i+1}(t)$. Similarly, for the last channel (i = N), where

there is no subsequent channels, the expression is simplified to $x_{i-1}(t)x_i(t)$. For all other intermediate array channels $2 \leq i \leq N-1$ the interpretation for equation 8 stands. The modification introduced by equation 8 is anticipated to reduce the computational cost, since the pairwise multiplication of RX signals is restricted by LCR. Once computed, the updated RX signals $y_{DMAS2-LCR}$ are sent to eq. 6 in order to extract the reconstructed image.

E. LCR Implementation on DMAS3 Processing Algorithm

An extension to the standard DMAS2 processing was proposed in [27] aiming at improving signal coherence by replacing pairwise multiplication for RX signals with the multiplication of triplets of RX signals, denoted as DMAS3 processing, defined by the following expression:

$$y_i^{DMAS3}(t) = \sum_{i=1}^{N-2} \sum_{j=i+1}^{N-1} \sum_{k=j+1}^{N} x_i(t)x_j(t)x_k(t) \quad (9)$$

Similarly to DMAS2 beamforming, in DMAS3 all possible triplets of RX signal envelopes are multiplied together prior to the summation. The application of eq. 9 excludes the RX signals from the last two channels given the lack of a consecutive triplet of RX signals. Similarly to DMAS2-LCR, the Localised Coherence Rule can be applied here to restrict multiplications of three consecutive signals to only RX signals from neighbouring channels located one-pitch and two-pitch distances apart. As a result, eq. 9 is optimised as seen below:

$$y_i^{DMAS3-LCR}(t) = \sum_{i=2}^{N-1} (x_{i-1}(t)x_i(t)x_{i+1}(t) + x_{i-2}(t)x_i(t)x_{i+2}(t)) \quad (10)$$

Specifically, the first pMUT channel (i = 1) does not have any preceding pMUT channel, and, hence, the term for the first position is null. The second pMUT channel (i = 2) has only one preceding pMUT channel, hence the term is solely $x_i(t)x_{i-1}(t)x_{i+1}(t)$. Eq. 10 is applicable for the remaining pMUT channels up to (and excluding) the second-to-last pMUT channel. Having only one following channel, the term for the second-to-last pMUT channel would be defined as: $x_{i-1}(t)x_i(t)x_{i+1}(t)$). For the last pMUT channel ($i = N$), given there is no following channel, the corresponding term is null. The updated RX signals $y_{DMAS3-LCR}$ are subsequently fed to eq. 6 to obtain the reconstructed image.

For DAM-LCR, DMAS2-LCR and DMAS3-LCR, the reconstructed 2D image is normalized by the maximum intensity within the 2D grid. It is worth noting that for all the image reconstruction algorithms discussed in this work, the pMUT directivity is incorporated in the post-processing algorithm to ensure that the pMUT FoV is taken into account in the final imaging result.

III. pMUT ARRAY CHARACTERISTICS

Figure 7 shows the optical image of the double-die pMUT array used in this work. The 6.5 MHz pMUT array consists

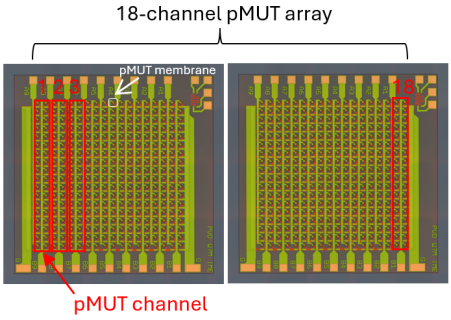

Fig. 7. Optical image of the 2D pMUT array

of 18 channels with two identical dies of 9 channels each wirebonded next to each other with every channel consisting of 36 (2 columns/channel × 18 membranes/column) membranes/channel. Each 80μm-wide membrane is comprised of a 4 μm-thick epi-polysilicon elastic layer and 2 μm-thick PVD PZT transducer layer sandwiched between Platinum (Pt) electrodes. The two dies are wirebonded on a PCB, which is placed in a tank filled with Fluorinert FC-70 (i.e., a low-loss liquid, whose acoustic impedance, Z is matching that of human tissues (equal to 1.3 MRayls)). For the pMUT actuation and data acquisition the Verasonics platform (Verasonics Vantage 64 system) is used with all channels being actuated with a 5-cycle sinusoidal waveform.

Initially, the FoV was determined through simulations (in COMSOL Multiphysics) with the actuating aperture consisting of either a single pMUT membrane or two membranes in line (denoted as dual-membrane pMUT aperture for the remaining of this document). Figure 8(a) depicts the normalised output pressure distribution in a polar plot. It can be observed from this plot that the FoV for a single pMUT membrane is equal to 180^o (considering the -3dB mark). Figure 8(b) shows the normalised output pressure distribution for the dual-membrane pMUT aperture with the FoV as expected dropping to 30^o.

To verify the observations on the FoV for the dual-membrane pMUT aperture from the simulated data, experimental chracterisation of a single pMUT channel (corresponding to a dual-membrane pMUT aperture). The device was measured experimentally in immersion (FC-70) using a 40 μm diameter hydrophone needle from Precision Acoustics Ltd. The die and hydrophone needle were placed in a pitch-catch arrangement with the Verasonics platform (Verasonics Vantage 64 system) used for the actuation of the pMUT channel. On reception, the hydrophone needle would move after each measurement point in order to raster-scan the (x,z) space above the pMUT channel and measure the RX time-domain pressure. The pMUT channel was actuated with a 16Vpp 5-cycles sinusoidal wave at the resonance frequency. Figure 9(a) illustrates the curve of the FoV at half power as a function of distance measured with the hydrophone right above the pMUT array in line-of-sight.

It can be observed from Fig. 9(a) that as the distance between the hydrophone and the pMUT die increases, the FoV reduces from 60^o to 10^o with a mean of approximately 30^o, and, thus, matching the observation made from the simulation

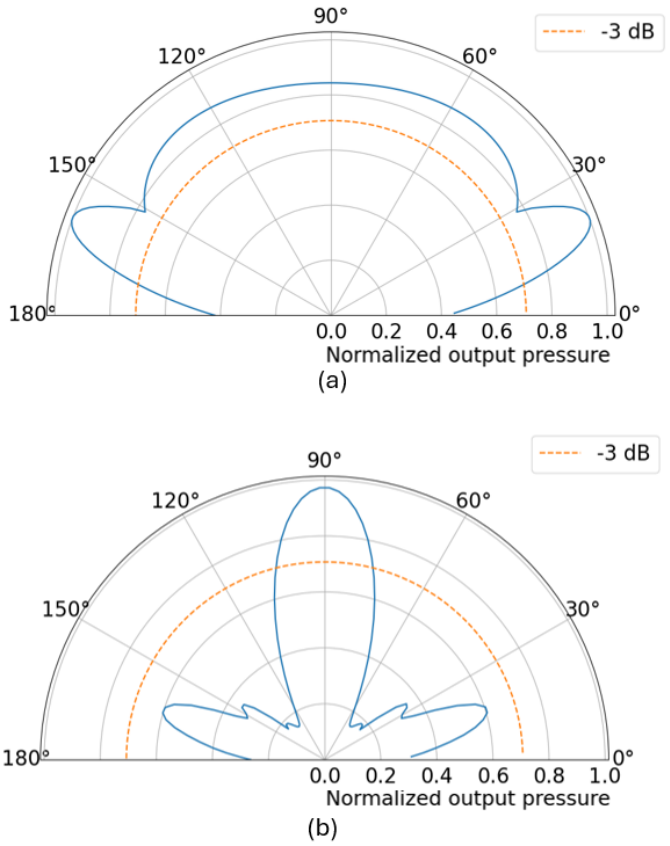

Fig. 8. Normalised output pressure distribution with angle (in ^{o}) measured at 20 mm for: (a) a single pMUT membrane aperture, and (b) a dual-membrane aperture.

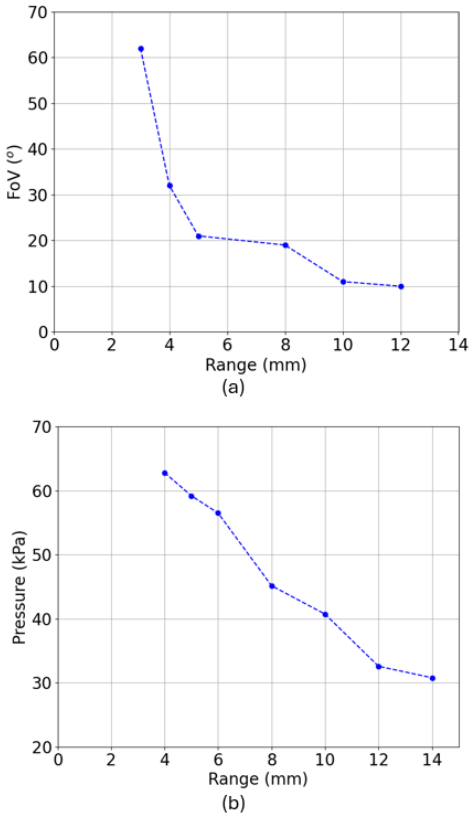

Fig. 9. (a) FoV at half power (in ^{o}), and (b) maximum pressure (in kPa) as a function of distance for a pMUT channel

work. Based on this observation, the FoV is restricted to 30^o by all the post-processing algorithms for the purposes of image reconstruction. Figure 9(b) depicts the trend of pressure emitted by a pMUT channel and measured by the hydrophone at various distances, when the hydrophone is placed in the line-of-sight to the pMUT channel. It can be argued that at ranges as close as 4 mm an impressive pressure (greater than 60kPa) is achieved by a single pMUT channel, setting the Tx pressure attained by the proposed 18-channel pMUT array (18*63 kPa = 1.08 MPa) to values greater than 1MPa at short ranges assuming the perfect coherent summation of the focused beams from all elements. Given that in reality potential beam incoherence would exist, it is expected that the actual total pressure achievable realistically from the phased array would be significantly less than the calculated value.

IV. Experimental Settings

Metal reflectors of different dimensions were used to validate in immersion the imaging performance of the proposed DAM-LCR, DMAS2-LCR and DMAS3-LCR against the classical DAS, DMAS2 and DMAS3 post-processing algorithms. Specifically, five experiments (denoted as A, B, C, D and E) with different reflector arrangements at different distances from the pMUT array were carried out. The sequence of the experiments is as follows: in Experiment A, a single 3 mm diameter spherical reflector was placed at 1 cm away from the narrow-FoV pMUT array, and roughly above the last pMUT channel, with the array actuated with first Common Source Method (CSM) followed by TX focusing in an attempt to highlight the advantage of using CSM specifically with narrow-FoV pMUTs.

In experiment B, the same 3mm diameter reflector was placed at 0.5 cm away from pMUT array at a central position considering first the proposed narrow-FoV 18-channel pMUT array (with every channel consisting of two columns of pMUT membranes) and then an 18-channel wide-FoV pMUTs of equivalent die design (with each channel comprising of a single column of pMUT membranes). This experiment aims at demonstrating why the proposed LCR concept is more effective with pMUT arrays with a narrow FoV. In Experiment C, a single 5 mm diameter spherical reflector 1 cm away from the array is considered. Experiment D challenges the imaging capability of the system by moving the reflector, which was used in the previous experiment, axially to determine the maximum range that the 18-channel array can still detect the reflector. In the Experiment E, the minimum attainable lateral resolution is established experimentally. Specifically, two identical 5 mm diameter spherical reflectors are placed 5 mm away from the array and close to each other, at a distance of 1.5mm to investigate whether they can be resolved by the aforementioned imaging algorithms.

Figures 10(a) to (e) illustrate the testing setup considered for Experiments A to E, respectively. In Fig. 10(d), the region of interest (ROI) marks (represented by the dashed

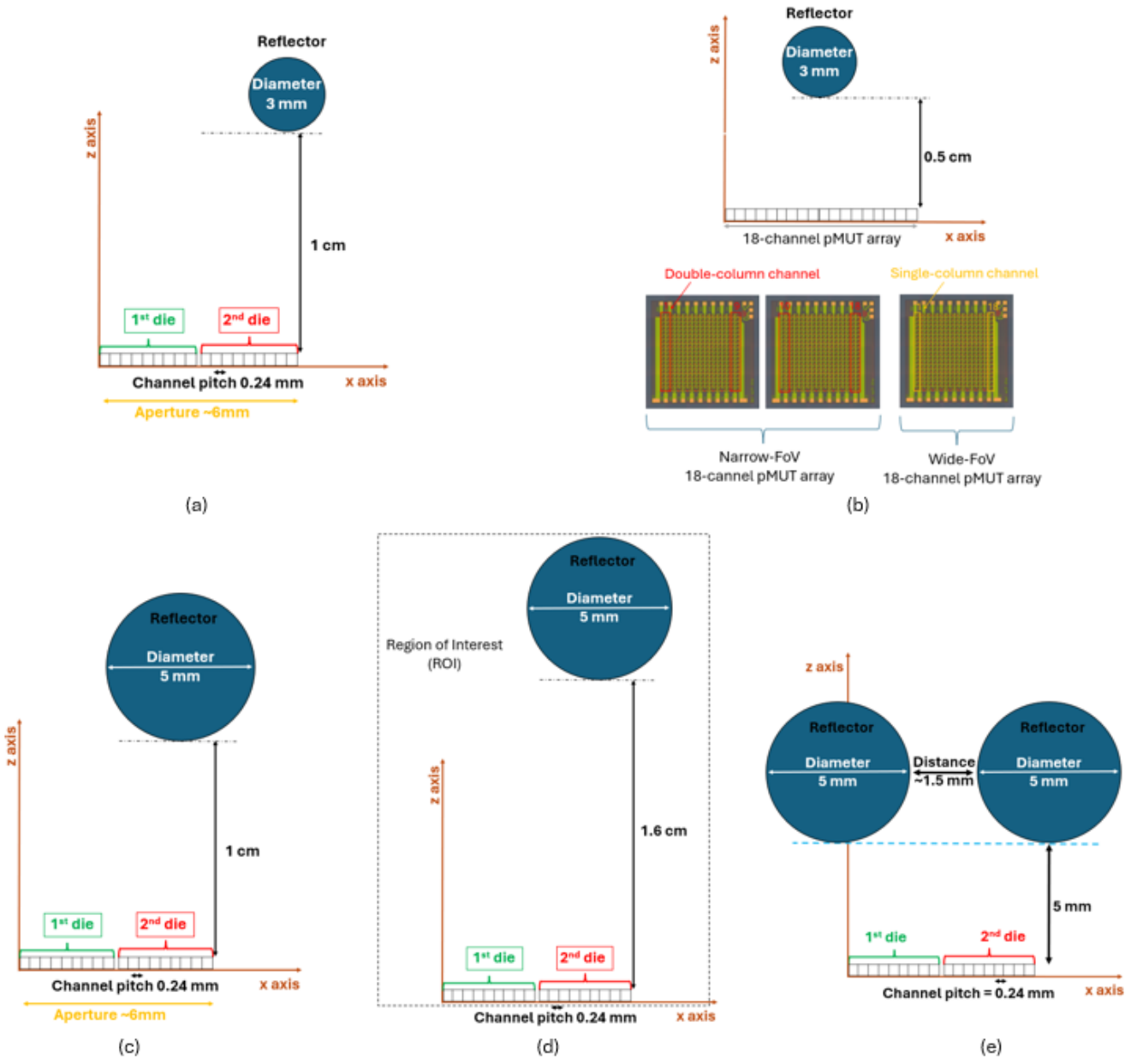

Fig. 10. Testing setup illustration for each experiment: (a) A 3 mm spherical reflector positioned 1 cm from the narrow-FoV pMUT array, tested with the Common Source Method (CSM) and TX focusing (Experiment A). (b) A 3 mm spherical reflector placed 0.5 cm from the pMUT array's center, comparing the double-column narrow-FoV 18-channel array with the single-column wide-FoV 18-channel array (Experiment B). (c) A 5 mm spherical reflector positioned 1 cm above the 2nd die of the narrow-FoV pMUT array (Experiment C). (d) A 5 mm spherical reflector placed 1.6 cm above the 2nd die of the narrow-FoV pMUT array (Experiment D). (e) Two identical 5 mm spherical reflectors spaced 1.5 mm apart, positioned 5 mm above the narrow-FoV pMUT array (Experiment E)

rectangular frame in this figure) the domain to be reconstructed by all the signal post-processing algorithms and corresponds to $x = [-1, 7]$ mm and $z = [0, 20]$ mm in the lateral and axial dimensions, respectively. Reconstruction of this ROI is considered consistently across all the experiments.

Apart from the reconstructed images for every algorithm, two metrics for benchmarking algorithm performance were considered in this work: (i) SNR, and (ii) the computational load for the execution of the code associated with every image reconstruction algorithm. Specifically, the SNR was calculated from the reconstructed image expressed by the following formula:

$$SNR(dB) = 10\log_{10}(\frac{P_S}{P_N}) \tag{11}$$

Parameter P_S corresponds to the signal power and is computed as the summation of intensity values for the pixels within a window denoting the location of the reflector, whereas P_N corresponds to the noise power and refers to the summation of energy intensity values for all the pixels located outside that window (i.e., the location of the reflector).

For all the results presented within this document, the FoV in the imaging algorithms was set to 30^o in order to approximate the measured pMUT FoV. As a result, the

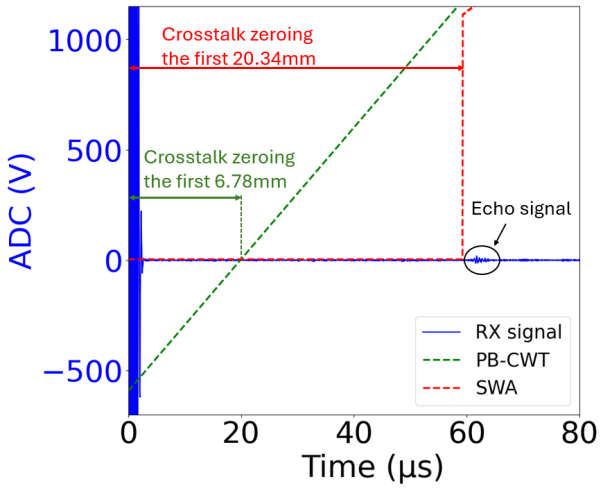

Fig. 11. Performance comparison in terms of crosstalk suppression between the proposed PB-CWT method and SWA algorithm

proposed image reconstruction algorithms apply a directivity constraint by verifying whether each pixel in the imaging domain falls within the pMUT channel's FoV, ensuring accurate reflector localization. In contrast, broad-FoV pMUTs arrays don't require this step, as the basic logic of the reconstruction algorithms provides correct localization on its own.

V. Evaluation of Proposed PB-CWT Method for Crosstalk Suppression

Initially, the proposed crosstalk suppression algorithm, PB-CWT, is evaluated considering measured data from a testing scenario, whereby a single cubic metalic reflector is immersed within the tank and placed above the pMUT array at a distance of approximately 1.6 cm (Experiment D). A comparison between the proposed PB-CWT method and the SWA algorithm proposed in [20] is provided here. Figure 11 depicts a time-domain RX signal and the implementation of both PB-CWT and SWA methods.

As depicted in Fig. 11, the tangent line to the signal phase (plotted in dashed green) crosses the x-axis resulting in zeroing the first 20 μsec of the RX signal, which corresponds to circa 6.8mm in range. Similarly, the offset sequence (plotted in dashed red), which is used by the SWA approach to determine the cutoff limit for the crosstalk zeroing, determines a blind zone of 60 μsec, which maps the crosstalk zeroing to approximately 2cm. As a consequence, the cutoff limit for SWA method is very close to the echo signal from the reflector. It can be argued that the proposed PB-CWT method outperforms the state-of-the-art, SWA approach, since it provides effective suppression of crosstalk while enabling the detection of reflectors as close as 6 mm, against the 20 mm attained with the SWA method, to the pMUT array in this testing scenario.

It is worth noting that the proposed PB-CWT method relies on a single measurement, thus, there is no need for a reference/template signal for calibration proposed in [12], [13]. On this basis, it can be argued that it is the most effective crosstalk suppression method for medical US imaging. Given that the in-body environment is dynamic, the capture of two consecutive signals sequentially under the same environmental conditions would be virtually impossible. On the contrary, SWA method is not robust against the dynamic intrabody changes. Moreover, SWA is slower computationally with the blind range (precisely defined by the offset sequence) depending on the distance of the reflector from the pMUT array. To sum-up, phase analysis in the form of the implementation of the proposed PB-CWT method, is more generic, faster and robust against environment variations, and can be applied in real-time by analysing the RX signal, from which crosstalk is to be mitigated.

Given the cross-talk's nature, it appears at the start of a capture (i.e., early-time contribution) and has very high peak-to-peak values (particularly when compared with the echo contribution), since from a propagation point-of-view it is less attenuated (compared to the echo signal). Furthermore, the cross-talk's characteristics are typically very similar across the RX data captured from adjacent channels, with equivalent amplitude and phase variations. The cross-talk contribution in this validation experiment could be effectively eliminated by identifying regions where the accumulated phase trend remains nearly stable rather than growing, as cross-talk contribution is significantly larger — by several orders of magnitude — than echoes from the reflector and background noise. In scenarios where the contrast between the echo and background noise is smaller than in the experiments discussed in this manuscript, the cross-talk suppression method should remain equally effective, as the cross-talk contribution continues to dominate over both the reflector echo and background noise.

VI. Validation of Proposed DAM-LCR Signal Processing Algorithm for Image Reconstruction

A. Analysis of Results

In Experiment A, a 3 mm diameter spherical reflector is placed above the second die (roughly above the last channel) at a distance of 1cm. The pMUT array was first actuated with CSM and reconstructed an image by feeding the RX data to the classical DAS processing. Then, the measurement was repeated by actuating the pMUT array with TX focusing at 1 cm (and roughly below the reflector) and again reconstructed an image by sending the RX data to the classical DAS processing. TX focusing is applied in this case across the lateral dimension, also known as focusing in the azimuthal direction. Figures 12(a) and (b) depict the RX signal from the last pMUT channel (which is expected to contain the strongest echo contribution) when considering CSM and TX focusing, respectively. Figs. 12(c) and (d) demonstrated the reconstructed images when considering each actuation mechanism.

In terms of individual RX signal strength for echo contributions, CSM results in approximately double the peak-to-peak signal amplitude compared to TX focusing, as shown in Fig. 12(a) and Fig. 12(b), respectively. This effect is reflected in the reconstructed images, where DAS processing was used to highlight the differences. Fig. 12(c) shows that CSM actuation produces better contrast quality and reduced background noise, with a maximum intensity of 450.3. In contrast, TX focusing

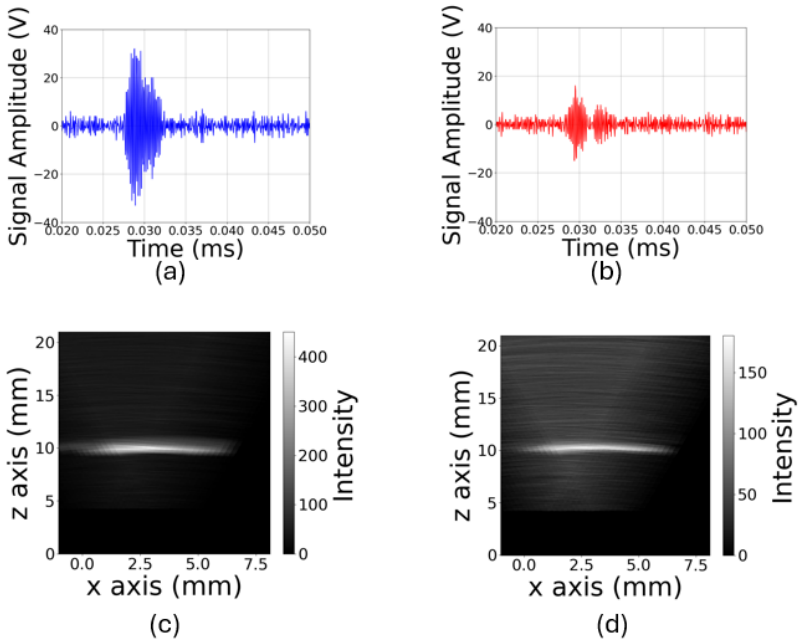

Fig. 12. RX signals at the last array channel for: (a) CSM and (b) TX focusing. Reconstructed images uaing DAS for: (c) CSM and (d) TX focusing. Experimental setup: a 3 mm spherical reflector positioned 1 cm from the narrow-FoV pMUT array, centered above the last channel (Experiment A)

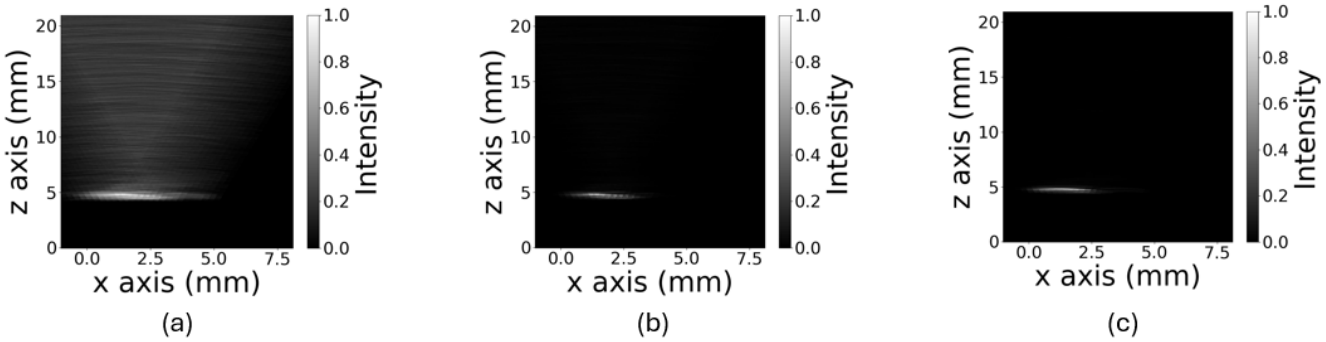

Fig. 13. Reconstructed images for (a) DAS, (b) DMAS3, and (c) DAM-LCR a single 3mm diameter spherical reflector 0.5 cm away from the double-column narrow-FoV pMUT array (Experiment B)

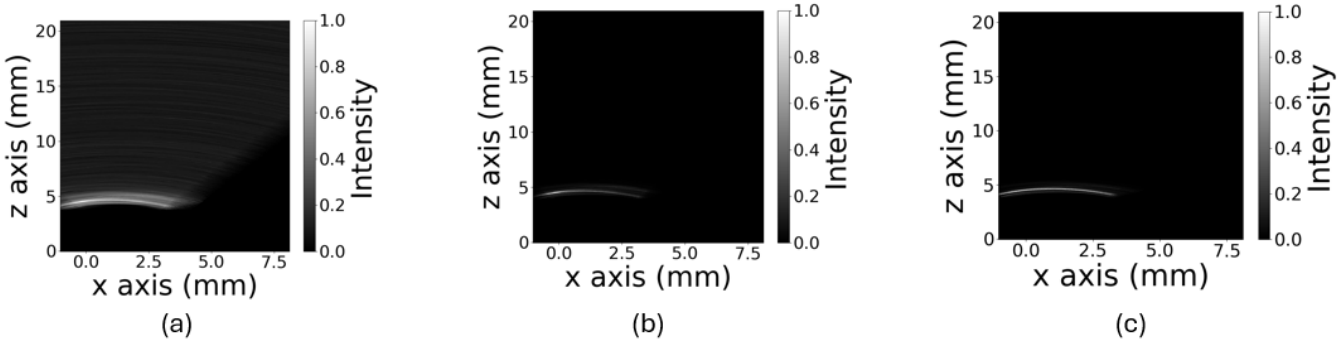

Fig. 14. Reconstructed images for (a) DAS, (b) DMAS3, and (c) DAM- LCR considering a single 3mm diameter spherical reflector 0.5 cm away from the single-column wide-FoV pMUT array (Experiment B)

results in a noisier reconstructed image, with a maximum intensity of 180.5 and significantly reduced contrast.

To quantify this difference, a new metric, namely the maximum-intensity ratio (MIR), is introduce, which is defined as:

$$MIR(dB) = 10\log_{10}(\frac{I_{max}^{CSM}}{I_{max}^{TXFoc}}) \quad (12)$$

where I_{max}^{CSM} is the maximum intensity obtained from the image reconstructed using DAS processing and considering CSM

TABLE I

SIGNAL-TO-NOISE RATIO (SNR) FOR DAS, DMAS3 AND DAM-LCR IMAGE RECONSTRUCTION ALGORITHMS BASED ON THE EXPERIMENTAL COMPARISON BETWEEN DOUBLE-COLUMN NARROW-FOV AND SINGLE-COLUMN WIDE-FOV PMUT ARRAYS

Image Reconstruction Algorithm	**SNR (dB)**	
	Double-column (narrow-FoV) array	***Single-column (wide-FoV) array***
DAS	4.3	6.1
DMAS3	10.5	11.7
DAM-LCR	12.1	11.9

for the actuation. Parameter I_{max}^{TXFoc} refers to the maximum intensity obtained from the image reconstructed using DAS processing and considering TX focusing for the actuation. Considering the reconstructed images in Figs. 12(c) and (d) which is approximately 4 dB. This highlights the significant advantage of CSM in terms of attainable maximum intensity compared to TX focusing.

It is worth highlighting here that elevation focusing for the specific phased array used in this work could be theoretically considered. Such focusing mechanism would be enabled through the horizontal wire-bonding of membranes to allow for the operation of channels in the elevation (vertical) dimension, thus, leveraging the gains of improved elevational resolution and minimized beamline height.

However, there are two reasons that such array functionality is not practically possible here. First, for the specifical die design used in this work, such horizontal wire-bonding is not feasible. Therefore, re-thinking of the phased array is required through careful re-designing of a chip to enable such operation, which is an aspect to follow-up in future pMUT array tape-outs. Second, elevation focusing could be employed to theoretically leverage lateral resolution gains by narrowing the beam width in the elevation dimension. However, the existing 3 mm width of the phased array would mean a very narrow coverage of the propagation domain along that dimension with the FoV varying depending upon how many rows of membranes are combined together to create a channel. If two rows are combined, then the narrow FoV on RX would result in reduced SNR (echoes scattered and not received by all the array channels) and, thus, leading to inadequate image reconstruction.

In Experiment B, an experimental comparison is introduced between the proposed 18-channel narrow-FOV array, where each channel consists of two columns of pMUT membranes (denoted as "double-column array") and an 18-channels pMUT array of an equivalent die design, where each channel consists of a single column of pMUT membranes (denoted as "single-column array"), and would, thus, have a broad FoV. A reflector corresponding to a 3mm diameter solid metal sphere was placed 0.5cm away from the array at a central position for each experiment. This experiment is introduced to demonstrate that the Localized Coherence Rule (LCR) is expected to be more effective for narrow FoV channels due to the uniformity of intersecting coverage. Since coherence enhancement relies on the uniformity of the overlapping channel coverage, applying the LCR to classical algorithms should achieve greater coherence improvement for narrow FoV pMUTs. For this experiment, only the classical DAS, DMAS3 and DAM-LCR image reconstruction algorithms are considered.

Figures 13(a)-(c) demonstrate the reconstructed images for the classical DAS, DMAS3 and the proposed DAM-LCR post-processing algorithms using the double-column pMUT array with a narrow FoV. Figures 14(a)-(c) shows the reconstructed images for the same post-processing algorithms using the single-column pMUT array with a wide FoV. Table I summarises the equivalent SNR values (in dB). In both Fig. 13 and 14, the noise level decreases, and SNR (from Table I) increases when transitioning from DAS to DMAS3, with improvements of 6.2 dB and 5.6 dB for the double-column and single column arrays, respectively. However, the SNR improvement from DAS to DAM-LCR is more pronounced in 13 (7.8 dB) compared to 14 (5.8 dB), supporting the theoretical assumptions outlined earlier.

For the narrow FoV pMUT array, the reflector contour in Fig. 13(b) appears aliased, with a lateral dimension of less than 3 mm (its actual physical size). In 13-(c), the reflector contour is more accurately represented, restoring it to its true 3 mm diameter. Conversely, in Figs. 14 (broad FoV pMUT), there is no significant difference in the lateral dimension of the reflector between Fig. 14(b) and 14(c). The only noticeable change is an increase in brightness (intensity) across the x-axis at the reflector's position.

In Experiment C (shown in Fig. 10), a spherical reflector with a 5mm diameter was immersed in the tank and positioned above the 1D narrow-FoV pMUT array. Specifically, the reflector was placed above the 2^{nd} die at a distance of 1 cm. Figures 15(a) to (f) demonstrates the reconstructed images relative to the single reflector experiment for all the post-processing algorithms considered in this benchmarking exercise. Table II provides a breakdown of the SNR values for each experiment along with the computational load for each evaluated image reconstruction algorithm in terms of number of operations (as a function of the number of operational array channels, N).

It can be argued that DMAS2 and DMAS3 image reconstruction algorithms, despite reducing the overall level of noise with respect to DAS processing, do not reconstruct correctly the full extent of the reflector in the lateral dimension (in particular along the x axis at x=[4,5] mm). As a consequence, DMAS2 and DMAS3 reconstructed images are affected by inaccurate reflector representation (reflector aliasing). This is attributed to the algorithmic logic of correlating pairs of RX signals from all channels that do not have an overlapping FoV. This is remedied through enhancing the traditional DMAS algorithms with LCR as depicted in the reconstructed images of the proposed DMAS2-LCR and DMAS3-LCR algorithms (Fig. 15(e) and (f)).

These modified algorithms result in image reconstructions that better represent the extent of the reflector in the lateral dimension. Similarly, the proposed novel DAM-LCR methodology results in a reconstructed image that provides an accurate representation of the lateral dimension of the reflector. Then the cross-section of the energy intensity within the reconstructed images (depicted in Figs. 15(a) to (f)) is

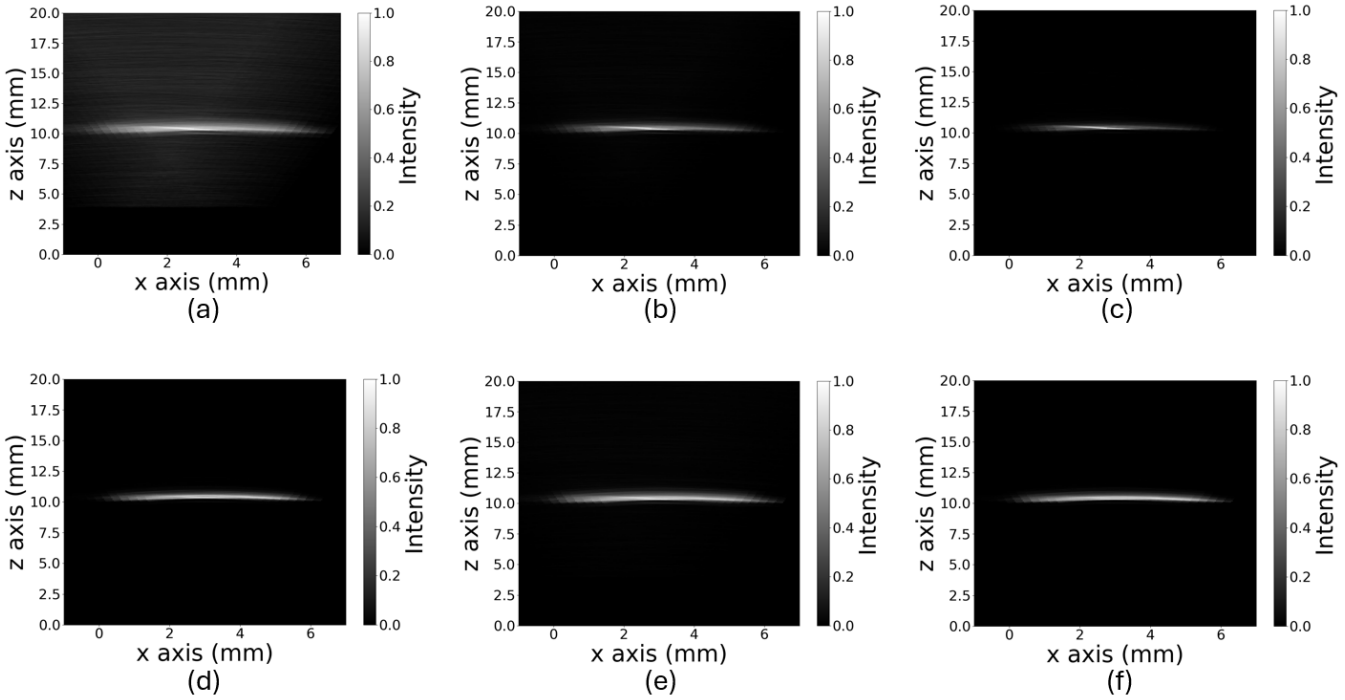

Fig. 15. Reconstructed images for (a) DAS, (b) DMAS2, (c) DMAS3, (d) DAM-LCR, (e) DMAS2-LCR, and (f) DMAS3-LCR considering a single 5 mm diameter spherical reflector 1 cm away from the pMUT array (Experiment C)

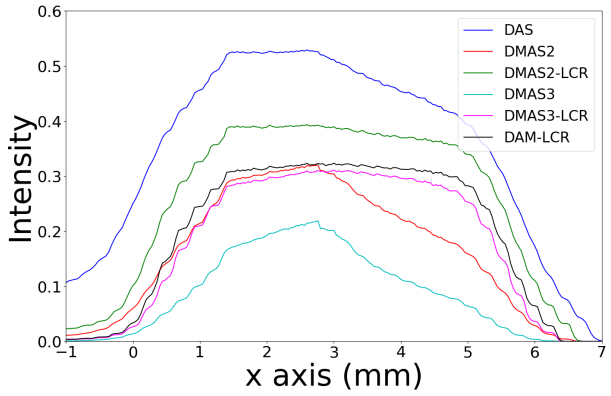

Fig. 16. Plot representation of the vertex information of the circular reflector by averaging the intensity values over a window in the z axis of -/+0.5 mm within the pixel of the maximum intensity for Experiment C

calculated by averaging the intensity values over an interval of -/+0.5 mm around the position of the maximum intensity along the z axis shown in Figure 16.

The plotted values in Fig. 16 represent the acoustic intensity localized at the bottom of the spherical reflector, which is the portion of the reflector most directly aligned with the pMUT's field of view. This region is the closest to the array and experiences near-normal incidence of the transmitted wave, resulting in the strongest reflections due to the large acoustic impedance mismatch at the liquid-metal interface. In other words, the bottom of the spherical reflector corresponds to the vertex information, which is the most prominent feature in the reconstructed image, consistent with classical Fresnel theory. Reflections from other parts of the spherical contour are weaker due to oblique incidence and phase cancellations, which is why they are less represented in the intensity plot.

By observing Fig. 16, it can be argued that the use of the classical DMAS2 and DMAS3 processing for narrow-FoV pMUT array is detrimental to the reconstructed lateral dimension of the reflector, particularly at the edge of the reflector ($x = [4, 5]mm$). Similarly to DMAS2 and DMAS3, DAS processing is also unable to resolve correctly the reflector edge. Despite being faster than DMAS2/3, the level of noise of DAS-reconstructed image is higher with respect to DMAS2/3. The intensity plot related to DAS considering the region, where the reflector is not present, has assigned intensity values set to zero in a less abrupt way with DMAS2/3. This is due to the lower level of coherence in DAS and DMAS2/3. On the contrary, the proposed DAM-LCR method can more accurately resolve the lateral dimension of the reflector at a lower computational cost with respect to DMAS2 and DMAS3. This observation is also applicable for the DMAS2-LCR and DMAS3-LCR processing algorithms, however at the expense of a much higher computational cost (i.e., DAM-LCR halves the computational cost compared to DMAS2-LCR and DMAS3-LCR).

In Experiment D, the same reflector is moved further away from the pMUT array at 1.6 cm, which is the maximum distance that echo signals are captured on RX (Experiment B). Figures 17(a) to (f) show the 2D reconstructed images considering each of the investigated signal post-processing algorithms. These images clearly demonstrate the superiority of LCR-based image reconstruction algorithms over traditional DAS and DMAS2 and DMAS3 methodologies when applied to pMUT arrays with a narrow FoV. LCR algorithms not only

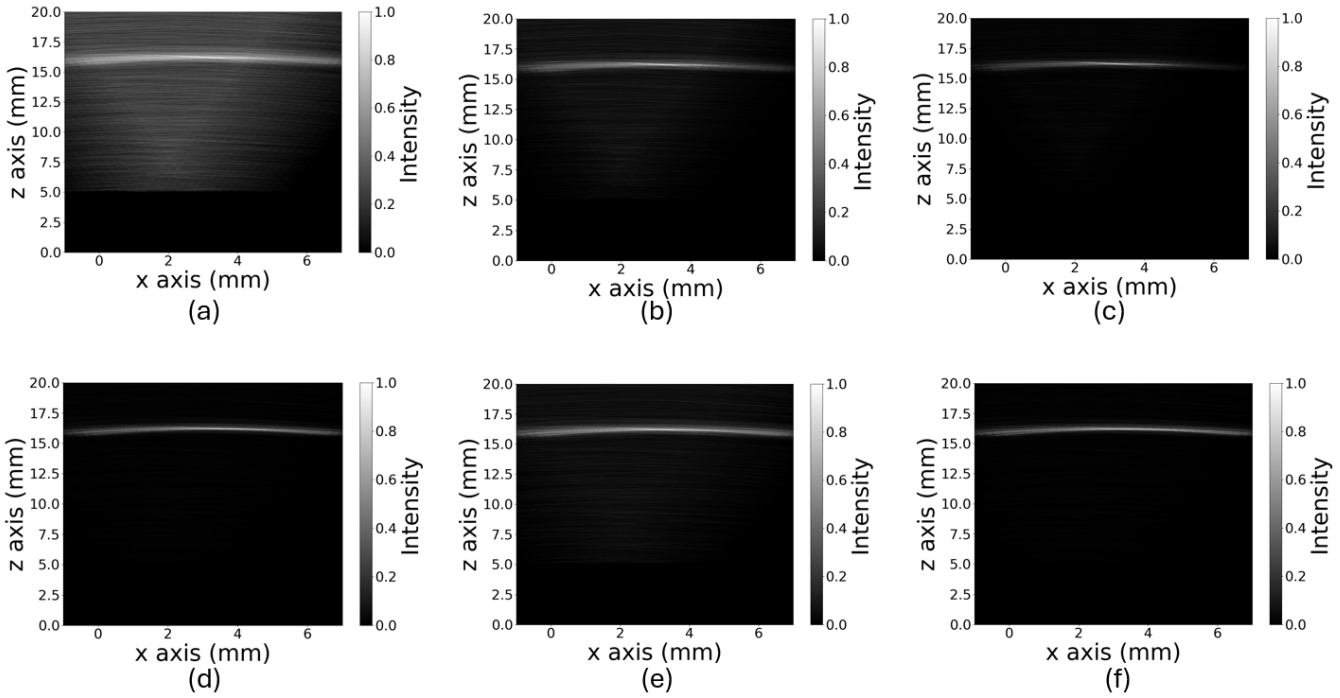

Fig. 17. Reconstructed images for (a) DAS, (b) DMAS2, (c) DMAS3, (d) DAM-LCR, (e) DMAS2-LCR, and (f) DMAS3-LCR considering a single 5 mm diameter spherical reflector 1.6cm away from the pMUT array (Experiment D)

provide a significant SNR boost but also eliminate reflector aliasing, which is present in traditional algorithms, while maintaining high levels of noise suppression but also reduce the computational cost with respect to traditional algorithms.

In the scenario depicted in Fig. 10(e), the two identical 5 mm diameter reflectors were placed at approximately 1.5mm to challenge the lateral resolution that could be achieved with the proposed pMUT array and DAM-LCR imaging scheme. Figures 18(a) to (f) show the 2D reconstructed images considering each of the investigated signal post-processing algorithms. It can be argued that the proposed DAM-LCR, DMAS2-LCR and DMAS3-LCR post-processing algorithms can more accurately distinguish between the two reflectors, by avoiding aliasing the extremities of the reflectors, while keeping the background noise to the minimum compared to the classical DAS, DMAS2 and DMAS3 processing methods. This is attributed to the RX signal multiplication employing the Localised Coherence Rule, which optimally relates the coverage of adjacent pMUT channels with a narrow FoV.

The effect of multiplications between all pairs of RX signals (introduced by the classical DMAS2 and DMAS3 processing) across spatially distant pixels in the intensity grid would result in the over-enhancement of signal coherence for narrow-FoV pMUT channels. Such over-enhancement would boost too much the intensity of the brightest pixels and suppress too much the intensity of the darkest pixels. This results on one side in distortions of the reconstructed image of the reflector and on the other side in reflector contour aliasing. Figure 19 corresponds to the plot of vertex information for the two adjacent circular reflectors in Experiment E, averaged over a ±0.5 mm window along the z-axis within the pixel of maximum intensity to demonstrate the ability of the proposed DAM-LCR methodology in achieving a lateral resolution of 1.5 mm considering a narrow-FoV pMUT array.

TABLE II

SIGNAL-TO-NOISE (SNR) RATIO AND COMPUTATIONAL LOAD METRICS FOR ALL IMAGE RECONSTRUCTION ALGORITHMS BASED ON EXPERIMENTAL DATA

Experiment	SNR (dB)			Computational Load (operations)
	C	***D***	***E***	
DAS	8.3	5.3	2.3	N^*
DMAS2	14.6	8.6	2.6	$\frac{N(N-1)}{2}$
DMAS3	20.4	11.9	2.5	$\frac{N(N-1)(N-2)}{6}$
DAM-LCR	21.2	13.8	9	$N-2$
DMAS2-LCR	15.8	9.2	5.8	$2N-2$
DMAS3-LCR	21.8	13.6	7.7	$2N-6$

*where N is the number of channels for the pMUT array.

Therefore, it is essential to limit the extent of signal multiplications suppressing the over-enhancement of signal coherence for these pMUT channels. Furthermore, the proposed DAM-LCR is outperforming DAS and DMAS2 processing in terms of clutter suppression as reflected in the SNR breakdown of Table I, while maintaining an optimum computational cost. Specifically, in the experiment encompassing two closely spaced reflectors (Exp. E), DAM-LCR more than triples the SNR compared to the state-of-the-art.

B. Discussion

It is worth highlighting that it is necessary to complement single-reflector with double-reflector experiments to demon-

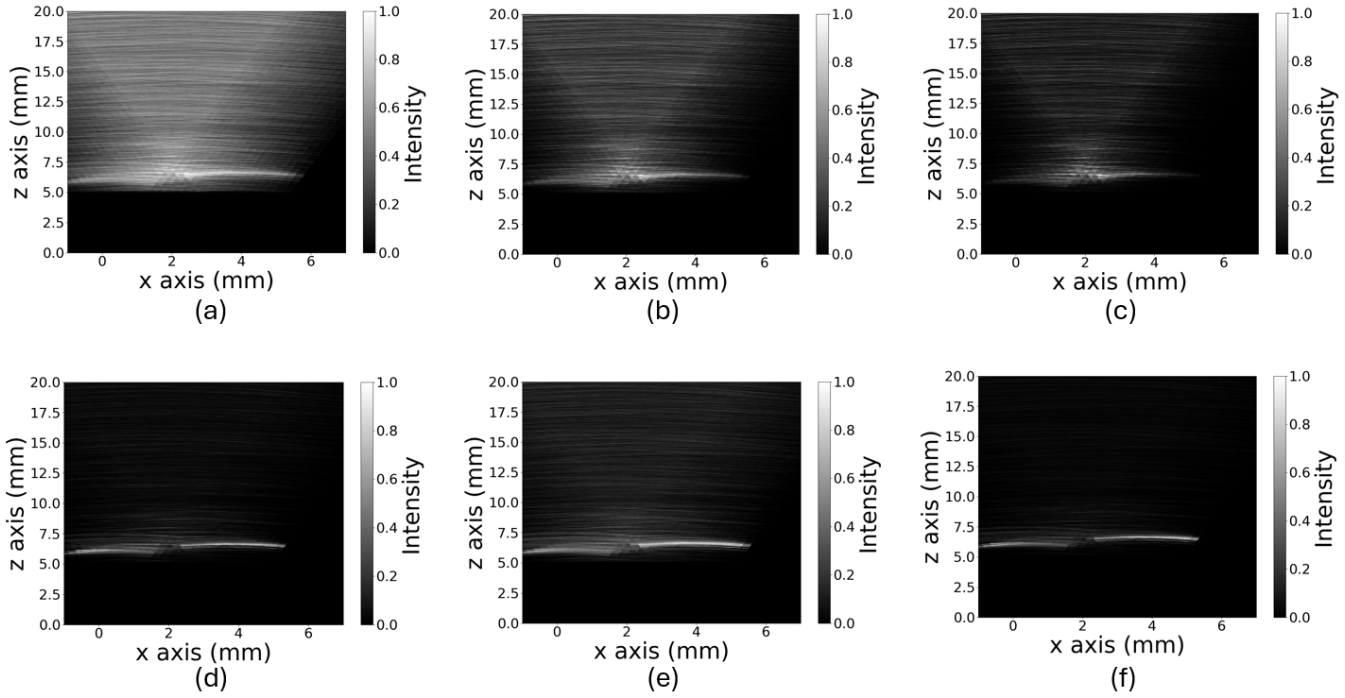

Fig. 18. Reconstructed images for (a) DAS, (b) DMAS2, (c) DMAS3, (d) DAM-LCR, (e) DMAS2-LCR, and (f) DMAS3-LCR considering two identical spherical 5 mm diameter reflectors placed approx. 1.5 mm apart 5 mm away from the pMUT array (Experiment E)

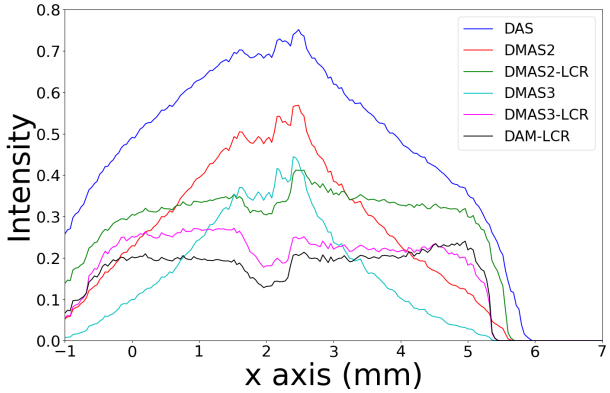

Fig. 19. Plot representation of the vertex information of the circular reflector by averaging the intensity values over a window in the z axis of -/+0.5 mm within the pixel of the maximum intensity for Experiment E

strate the real capability of the proposed image reconstruction algorithms. Furthermore, SNR is a Figure of Merit (FoM) that highlights the improvement in noise suppression from DAS to DMAS2 and DMAS3, as indicated by the correspondent increasing SNR values. However, the SNR FoM cannot demonstrate/showcase the effect of aliasing external parts of reflector typical of the classical DMAS3 with respect to DAM-LCR. The SNR of DAM-LCR and DMAS3 are nearly equivalent in Experiment A (single-reflector experiment) but these values are not fully representative of the differences between the DAM-LCR and the DMAS3 image reconstructions. The double-reflector experiment (Experiment E) is the demonstration of the effectiveness of the proposed DAM-LCR image reconstruction algorithm over the most advanced state-of-the-art image reconstrution algorithm (namely, DMAS3). Indeed, while DAM-LCR (measured computational cost equal to 7.5 sec) is approximately halving the computational time with respect to DMAS3 (measured computational cost equal to 16 sec), the SNR is more than 3 times higher than DMAS3. The SNR values for the reconstructed images of the DAS, DMAS2, DMAS3 algorithms are nearly equivalent in the two-reflectors experimental scenario. This is a demonstration that for narrow-FOV pMUTs, the logic of enhancing signal coherence by including multiplication between all the RX signals prior to summation is not effective. This benchmarking exercise demonstrates that solely DAM-LCR can resolve two distinct reflectors from background noise, achieving a 1.5 mm lateral resolution using narrow-FoV pMUT arrays (circa 30^o in this work) with an aperture as small as 10 mm$\times$10 mm, while keeping the post-processing computational cost to a minimum.

It is worth highlighting here that this work aims at investigating 2D imaging and the evaluation of the nominal lateral resolution of the system consisting of a small pMUT array with a narrow FoV. Hence, performing elevation focusing or focusing in the azimuthal direction was not within the scope of the work. Notwithstanding this consideration, elevation focusing (and/ or focusing in the azimuthal direction) can be pursued in the future as a possible investigation to validate the performance of a system with a suitably-wired pMUT array (in terms of resolution) both in the vertical (and/ or lateral) dimension.

The overall small dimensions and aperture size (below 6 mm) for the pMUT array used in this work are the two key parameters directly impacting the attainable image resolution. Notwithstanding these constraints, the proposed imaging scheme can significantly boost overall image SNR (seen in Table II) and lateral resolution (seen in Figs. 16 and 19) while

keeping a computational cost comparable to DAS (seen in Table II). Given the fact that the physical constraints of the aperture are dominating the effective resolution in the reconstructed images, it is recommended that future benchmarking work would be needed with larger aperture arrays to fully assess the performance advantages that can be leveraged from the proposed algorithm.

The focus of this work is towards potential intrabody medical applications, such as endoscopy or implantable devices. Thus, smaller arrays would be recommended over larger arrays. With this consideration in mind, the authors believe that future benchmarking is still required to evaluate both the array size suitability and the LCR rule along with the overall algorithm for image reconstruction in media mimicking such intra-body operation. This investigation will help identify physical constraints of the aperture that may limit the effective resolution in reconstructed images, while also assessing the algorithm's suitability for intrabody medical imaging and any necessary modifications required.

VII. Conclusion

The work presented here aims at introducing a novel signal pre-processing algorithm for crosstalk suppression, PB-CWT, along with a novel image reconstruction algorithm, DAM-LCR. These proposed methods are evaluated using measured data considering a narrow-FoV 6.5MHz PZT pMUT array with a 6mm$\times$6mm aperture. The proposed PB-CWT enables effective crosstalk suppression by significantly reducing the blind range with respect to the state-of-the-art crosstalk suppression signal processing methods (e.g., SWA, calibration) and could be implemented in dynamic environments, such as towards intrabody medical applications.

From the evalution of the proposed DAM-LCR method along with the state-of-the-art DAS, DMAS2 and DMAS3 processing algorithms it can be argued that for pMUT arrays with a narrow FoV, signal multiplication enhances signal coherence particularly when considering the Localised Coherence Rule. This is due to the fact that neighbour pMUT channels would have greater coverage intersection, and, thus, the multiplication of the respective received signals would naturally reach an optimum level of coherence. As a result, the reconstructed images from both simulated and measured data validate the superiority of the proposed DAM-LCR algorithm, comfortably achieving a 1.5mm lateral resolution with the highest SNR and lowest computational cost metrics with respect to the state of the art DMAS3 algorithm.

The results presented in this work indicate that such a narrow-FoV small form factor PZT pMUT array when paired with the novel proposed signal post-processing methods can extend the detectable range, while reducing the blind zone and, thus, have great potential for applications towards imaging in liquids such as medical diagnostics, medical therapeutics, etc.

Acknowledgment

This research was supported by A*STAR under "Piezo Specialty Lab-in-Fab 2.0" (Grant No. I2301E0027).

References

[1] Z. Qiu, Y. Lu, and Z. Qiu, "Review of ultrasonic ranging methods and their current challenges," Micromachines, vol. 13, no. 4, p. 520, 2022.
[2] Y. Koh, et al., "High resolution, high frequency ultrasonic ranging in air with pmuts," in 2021 IEEE International Ultrasonics Symposium (IUS). IEEE, 2021, pp. 1–4.
[3] W. Lee and Y. Roh, "Ultrasonic transducers for medical diagnostic imaging," Biomedical engineering letters, vol. 7, no. 2, pp. 91–97, 2017.
[4] C. Holmes, B. W. Drinkwater, and P. D. Wilcox, "Post-processing of the full matrix of ultrasonic transmit–receive array data for non-destructive evaluation," NDT & e International, vol. 38, no. 8, pp. 701–711, 2005.
[5] Y Yu, A Safari, X Niu, B Drinkwater, KV Horoshenkov, "Acoustic and ultrasonic techniques for defect detection and condition monitoring in water and sewerage pipes: A review", - Applied Acoustics, 2021.
[6] I. Rakkolainen, E. Freeman, A. Sand, R. Raisamo and S. Brewster, "A Survey of Mid-Air Ultrasound Haptics and Its Applications," in IEEE Transactions on Haptics, vol. 14, no. 1, pp. 2-19, 1 Jan.-March 2021.
[7] W. Ji, et al., "Total-focus ultrasonic imaging of defects in solids using a pzt piezoelectric micromachined ultrasonic transducer array," IEEE Transactions on Ultrasonics, Ferroelectrics, and Frequency Control, vol. 68, no. 4, pp. 1380–1386, 2020.
[8] Y. Qiu, et al., "Piezoelectric micromachined ultrasound transducer (pmut) arrays for integrated sensing, actuation and imaging," Sensors, vol. 15, no. 4, pp. 8020–8041, 2015.
[9] O. Rozen, et al., "Monolithic mems-cmos ultrasonic rangefinder based on dual-electrode pmuts," in 2016 IEEE 29th International Conference on Micro Electro Mechanical Systems (MEMS). IEEE, 2016, pp. 115–118.
[10] Y. Zhang, C. Huang and H. Gao, "Design of AlN and PZT pMUT for high-quality ultrasound imaging," 2021 IEEE International Ultrasonics Symposium (IUS), Xi'an, China, 2021, pp. 1-3.
[11] F. S. Foster, L. K. Ryan and D. H. Turnbull, "Characterization of lead zirconate titanate ceramics for use in miniature high-frequency (20-80 MHz) transducers," in IEEE Transactions on Ultrasonics, Ferroelectrics, and Frequency Control, vol. 38, no. 5, Sept. 1991, pp. 446-453.
[12] M. Sarafianou, D. S. W. Choong, D. J. Goh, D. S. -H. Chen and Z. Yao, "A CSM/TFM imaging scheme for Silicon-On-Nothing ScAlN pMUT arrays," 2022 IEEE International Ultrasonics Symposium (IUS), Venice, Italy, 2022, pp. 1-4.
[13] M. Sarafianou et al., "Long-Range High-Resolution Imaging With Silicon-on-Nothing ScAlN pMUTs," in IEEE Sensors Journal, vol. 23, no. 20, pp. 24254-24263, 15 Oct.15, 2023.
[14] H. Li et al., "An extension of double-stage DMAS for PMUT array imaging," 2022 IEEE International Ultrasonics Symposium (IUS), Venice, Italy, 2022, pp. 1-3.
[15] Y. Lu, H.-Y. Tang, S. Fung, B. E. Boser, and D. A. Horsley, "Pulse-echo ultrasound imaging using an aln piezoelectric micromachined ultrasonic transducer array with transmit beam-forming," Journal of Microelectromechanical Systems, vol. 25, no. 1, pp. 179–187, 2015.
[16] Y. Lu, H. Tang, Q. Wang, S. Fung, J. M. Tsai, M. Daneman, B. E. Boser, and D. A. Horsley, "Waveguide piezoelectric micromachined ultrasonic transducer array for short-range pulse-echo imaging," Applied Physics Letters, vol. 106, no. 19, p. 193506, 2015.
[17] R. A. Esteves, S. Sadeghpour and M. Kraft, "A Multiple Algorithm Imaging Scheme Towards In-Vitro Reconstruction Performance Benchmarking for pMUTs," 2023 IEEE International Ultrasonics Symposium (IUS), Montreal, QC, Canada, 2023, pp. 1-4.
[18] S. Sadeghpour, E. Zilonova, J. D'Hooge and M. Kraft, "A Novel 6 MHz Phased Array Piezoelectric Micromachined Ultrasound Transducer (pMUT) with 128 Elements for Medical Imaging," 2021 IEEE International Ultrasonics Symposium (IUS), Xi'an, China, 2021, pp. 1-4.
[19] R. Y. Chiao and L. J. Thomas, "Analytic evaluation of sampled aperture ultrasonic imaging techniques for nde," IEEE transactions on ultrasonics, ferroelectrics, and frequency control, vol. 41, no. 4, pp. 484–493, 1994.
[20] M. Sarafianou, et al., "Preliminary evaluation of multi-angle spatial compound imaging with pMUTs", to be presented at IEEE Sensors 2024 Conference, Kobe, Japan, 2024.
[21] Prasad, L., & Iyengar, S.S. (1997). Wavelet Analysis with Applications to Image Processing (1st ed.). CRC Press.
[22] C. -H. Chuan, S. Vasana and A. Asaithambi, "Using Wavelets and Gaussian Mixture Models for Audio Classification," 2012 IEEE International Symposium on Multimedia, Irvine, CA, USA, 2012, pp. 421-426.
[23] M. Sarafianou, et al., "Application of Continuous Wavelet Transform for time-of-Flight Ranging Applications Using air-Coupled pMUTs", to be presented at IEEE IUS 2024 Conference, Taipei, Taiwan, 2024.

[24] Ward, et al., “Morlet Wavelet Filtering and Phase Analysis to Reduce the Limit of Detection for Thin Film Optical Biosensors.”, ACS Sens. (2021).
[25] J.-F. Deprez, M. Sarafianou, M. Klemm, I. J. Craddock, and P. J. Probert-Smith, ”Microwave Contrast Imaging of Breast Tissue from Local Velocity Estimation,” Progress In Electromagnetics Research B, Vol. 42, 381-403, 2012.
[26] H. B. Lim, N. T. T. Nhung, Er-P. Li, and N. D. Thang, “Confocal microwave imaging for breast cancer detection: delay-multiply-andsum image reconstruction algorithm,” IEEE Transactions on Biomedical Engineering, vol. 55, pp. 1697-1704, June 2008.
[27] L. Eslami, F. Makouei, M. S. Ziksari, S. A. S. Karam and B. M. Asl, ”A new extension of DMAS ultrasound nonlinear beamformer using the third degree terms with low computational complexity,” 2021 IEEE International Ultrasonics Symposium (IUS), Xi’an, China, 2021, pp. 1-4.

Gaia Giubilei is a Master’s student at Politecnico di Torino, specializing in Micro and Nanotechnologies for Integrated Systems. She is completing her Master’s thesis at the Institute of Microelectronics (IME) in Singapore, focusing on receive beamforming algorithms with Piezoelectric Micromachined Ultrasonic Transducers (pMUTs) for ultrasound imaging. In 2023, she interned at Northeastern University, USA, working on Metamaterial Absorbers and MEMS resonant infrared detectors for gas sensing. In 2021, she gained experience in Heterodyne Interferometry during an internship at the National Institute of Metrological Research (INRiM), Italy, as part of the Next Generation Gravity Mission (NGGM) project with the European Space Agency (ESA). She holds a Bachelor’s degree in Physical Engineering (2022) from Politecnico di Torino, with research interests in neuroprosthesis and bio-magnetic field detection for neurodegenerative diseases.

Mantalena Sarafianou is a Scientist at the Institute of Microelectronics (IME), a research institute of the Agency for Science, Technology and Research (A*STAR) in Singapore. Her current research interests are in signal processing applications for ultrasonic miniaturized sensors. Dr Sarafianou has experience of working as an R&D engineer, specialising in the development of signal processing solutions for a wide range of industries such as medical devices, consumer electronics, and automotive.

Dr Sarafianou is an alumna of the University of Bristol, where she obtained a postgraduate degree in Communication Systems and Signal Processing (MSc: 2008), and a doctorate in in Electrical and Electronic Engineering (PhD: 2012), and the Aristotle University of Thessaloniki, Greece, where she completed her undergraduate degree in Electrical and Computer Engineering (2007).

David Sze Wai Choong graduated from the National University of Singapore with a Honours degree, Bachelor of Engineering (Mechanical) in 2015 and proceeded to work in the semiconductor manufacturing industry for 2 years before joining A*STAR, Institute of Microelectronics (IME) in 2017. He has spent 3 years in the MedTech department working on miniaturized medical devices on silicon for catheter integration and on flexible electronics and sensor integration for biomedical, applications. Currently, he is working under the MEMS department and acoustics group to further research MEMs PMUT devices in terms of performance testing, data analysis and prototyping applications.

Duan Juan Goh is a research engineer at Institute of Microelectronics, Agency for Science, Technology and Research (A*STAR). He graduated from Nanyang Technological University with degree in Mechanical Engineering in 2020. Despite being fairly new to the field, his research work has involved testing related studies in MEMS technology, including pMUTs, resonators, wake-up sensor switches.

Yul Koh is a Senior Scientist at the Institute of Microelectronics (IME), a Research Institute under the Agency for Science, Technology and Research (A*STAR) in Singapore. He graduated in 2015 from the Department of Electrical and Electronic Engineering at Seoul National University, South Korea. Yul began his research career at LG Electronics’ Sensor Solution Lab, where he specialized in the development of MEMS sensor platforms and their integration into commercial products. In his current role at IME, he focuses on acoustic MEMS devices, particularly in the areas of piezoelectric micromachined ultrasound transducers (PMUTs) and low-power MEMS switches.